Toward scalable ion traps for quantum information processing

J M Amini[1,5], H Uys[2], J H Wesenberg[3], S Seidelin[4], J Britton, J J Bollinger, D Leibfried, C Ospelkaus, A P VanDevender and D J Wineland

National Institute of Standards and Technology, Time and Frequency Division, 325 Broadway, Boulder, CO 80305, USA
E-mail: Jason.Amini@gtri.gatech.edu

Abstract. In this paper, we report the design, fabrication and preliminary testing of a 150 zone ion trap array built in a 'surface-electrode' geometry micro-fabricated on a single substrate. We demonstrate the transport of atomic ions between the legs of a 'Y'-type junction and measure the *in-situ* heating rates for the ions. The trap design demonstrates the use of a basic component design library that can be quickly assembled to form structures optimized for a particular experiment.

S Online supplementary data available from stacks.iop.org/NJP/12/033031/mmedia

---

[1] Present address: Georgia Tech Quantum Institute, GTRI/STL, CRB Building, 400 10th Street NW, Atlanta, GA 30318, USA.

[2] Present address: Council for Scientific and Industrial Research, Meiring Naudé Road, Brummeria, Pretoria, South Africa.

[3] Present address: Centre for Quantum Technologies, National University of Singapore, 117543 Singapore.

[4] Present address: Institut Neel-CNRS, BP 166, 25, rue des Martyrs, 38042 Grenoble Cedex 9, France.

[5] Author to whom any correspondence should be addressed.

IOP Institute of Physics · **Φ** DEUTSCHE PHYSIKALISCHE GESELLSCHAFT

Contents

1. Introduction

The basic components of a quantum information processor using trapped ions have been demonstrated in a number of experiments [1–3]. To perform complex algorithms that are not tractable with classical computers, these components need to be integrated and scaled to larger numbers of quantum bits (qubits). Both integration and scaling can be achieved by making trap arrays with many zones. In one possible scheme, information is shared between zones by physically transporting the ions between trapping zones that have various specialized functions such as detection, storage and logic gates [4–6]. We report here on the design, fabrication and preliminary testing of a large array built in a 'surface-electrode' geometry [7, 8] and report the first transport of atomic ions through a surface-electrode trap junction. Transport of ions through a junction has been demonstrated previously in multi-layer (three-dimensional) trap electrode geometries [9, 10]. The surface-electrode trap described here is composed of 150 zones and six 'Y' type junctions and is in principle scalable to an arbitrarily large number of zones. It demonstrates the use of a basic component design library that can be quickly assembled to form structures designed for a particular experiment or, in the future, a particular algorithm. Microfabricated on a single substrate, the traps are amenable to rapid mass fabrication.

Ion trap design, fabrication and characterization for quantum information experiments can be a difficult and time-consuming process. With a design library and fabrication techniques as demonstrated in this paper, we illustrate the use of pre-designed and pre-characterized, modular components that can be assembled into trap designs for specific experiments. The design library includes components for Y junctions, loading, transport and generic 'experiment' regions. We combined six of the Y junctions into a hexagonal ring that includes two loading components and two experiment regions, as shown in figure 1. Fabrication of five of the unmounted traps on a single 76 mm diameter wafer took one week.

The ion trap described in this paper and shown in figures 1(a) and (b) is a planar version (surface-electrode trap) of a radio-frequency (rf) Paul trap [7, 8] that confines ions by combining a ponderomotive potential generated by an rf electric field and static electric potentials, as shown in figure 2. In the configuration shown in figure 1, the ponderomotive potential (also called the pseudopotential) does not form a fully three-dimensional trapping potential. Instead, it forms a
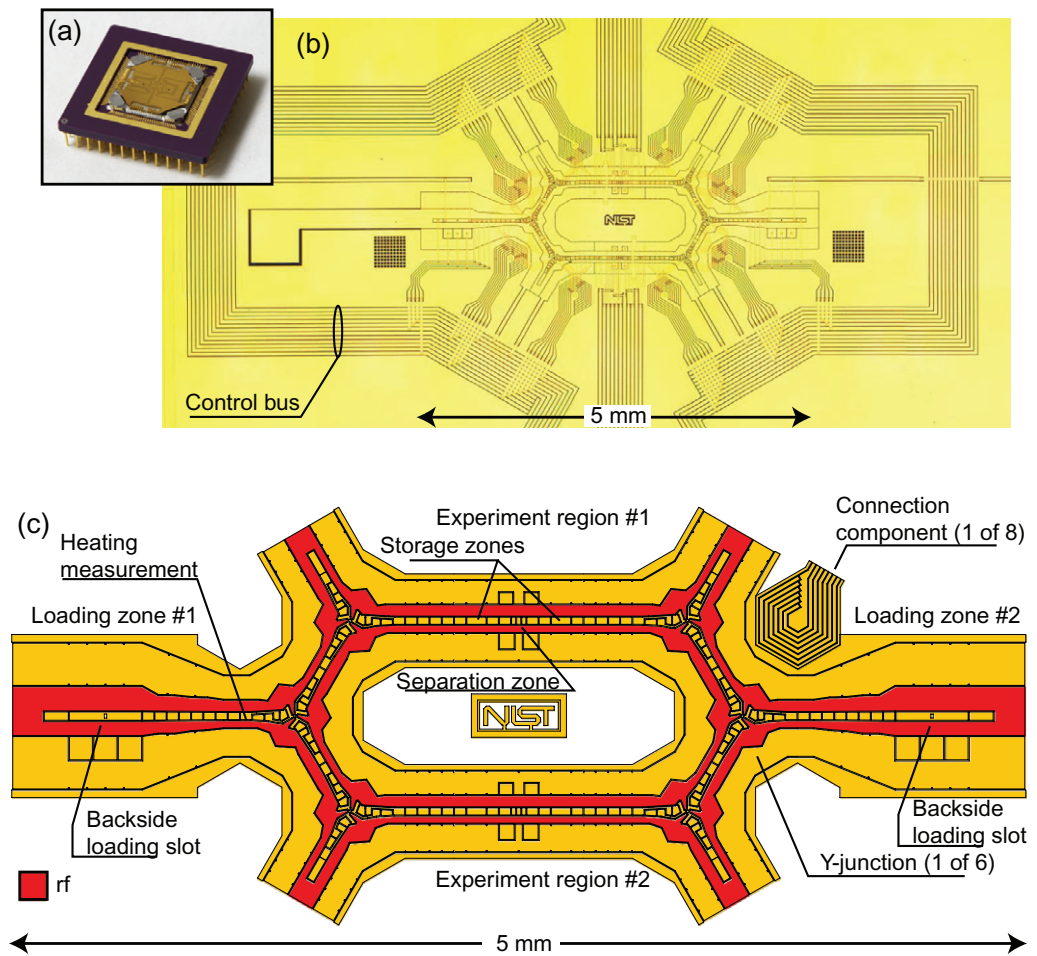
Figure 1. Photographs of (a) the trap mounted in a 120 pin PGA (pin grid array) carrier and (b) the active region of the fabricated trap. The design of the trap electrodes is shown in (c). This design features 150 transport/storage/probing zones, six Y junctions, and separation regions in the top and bottom paths of the hexagon. The trapping regions and the control bus are connected using standardized connection components that sit in crooks of the Y junctions. Future designs could scale the structure by repeating the hexagonal pattern or could create new patterns using the same component library.

confining tube and static or slowly varying control potentials applied to segmented electrodes confine ions along the axis of the tube(s). By changing the control potentials slowly with respect to the rf period, the ions can be smoothly transported along the tube. For added versatility, the trap includes junctions that combine multiple ponderomotive tubes and allow the ions to switch between multiple paths.

2. Fabrication

The trap fabrication is based on gold-on-quartz structures reported in [7, 8], where a quartz wafer (which has low rf loss) is coated with a patterned gold conducting layer. The monolithic
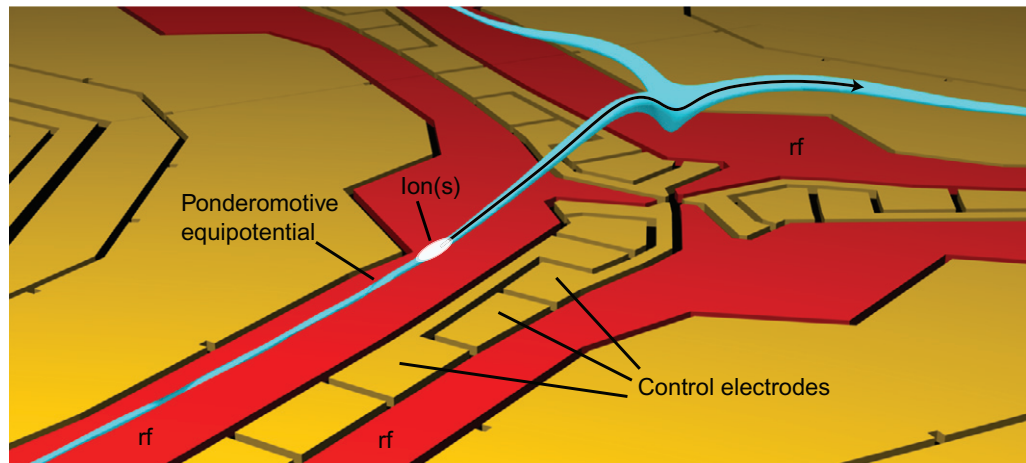
Figure 2. Example rf ponderomotive potential contour. For the experimental conditions used when testing the trap (51 V peak rf at 90.7 MHz and trapping ^{24}Mg$^+$), this contour corresponds to 1.3 meV. By changing the potentials on the control electrodes, the ion is moved along the two-dimensional confining tube formed by ponderomotive potential. Junctions join multiple tubes and the control potentials move the ion between the junction's legs.

construction of surface-electrode traps provides a basis for scalable ion trap structures. However, as the trap complexity increases, distributing the potentials to the control electrodes becomes increasingly difficult. The design of the trap described here could not be realized using a single conducting layer because control electrodes between the rf 'rails' form isolated islands surrounded by other control electrodes. To counter this problem, we extended the single conducting layer fabrication used in [8] to multiple conducting layers, as shown in figure 3(a). The top conducting layer forms a nearly continuous conducting plane that shields the ion from the potentials on the second (lower) conducting layer (see [11]).

The fabrication process begins with a 380 μm thick amorphous quartz wafer. The first conducting layer is 300 nm of evaporated Au with 20 nm Ti adhesion layers deposited on both sides of the Au. These layers are lithographically patterned and etched (wet etched for Au and plasma etched for Ti) to form the interconnects (figure 3). A 1 μm layer of SiO$_2$ is then deposited by chemical-vapor deposition, forming the insulation between the two layers. The Ti layer deposited on top of the Au acts as an adhesion layer for this oxide. The top conducting layer is 1 μm of evaporated Au with a 20 nm Ti adhesion layer, patterned using the liftoff technique [12]. Holes etched through the oxide, here denoted as vias, allow electrical connections to be deposited between metal layers. The vias are plasma etched with a process that results in sloped side walls by laterally etching the photoresist at the same rate as the oxide is etched. Because the liftoff technique, used for the top layer of Au, requires a directional flux of Au during the deposition, vias with a vertical side wall would not necessarily have the walls coated with Au, resulting in electrical discontinuities between the two conducting layers.

The trap was loaded by passing a neutral flux of ^{24}Mg through slots in the wafer. To form these slots, tapered channels through the quartz wafer were mechanically drilled from the back side of the wafer to within 30 μm from the top front surface at locations under the two loading

(a)
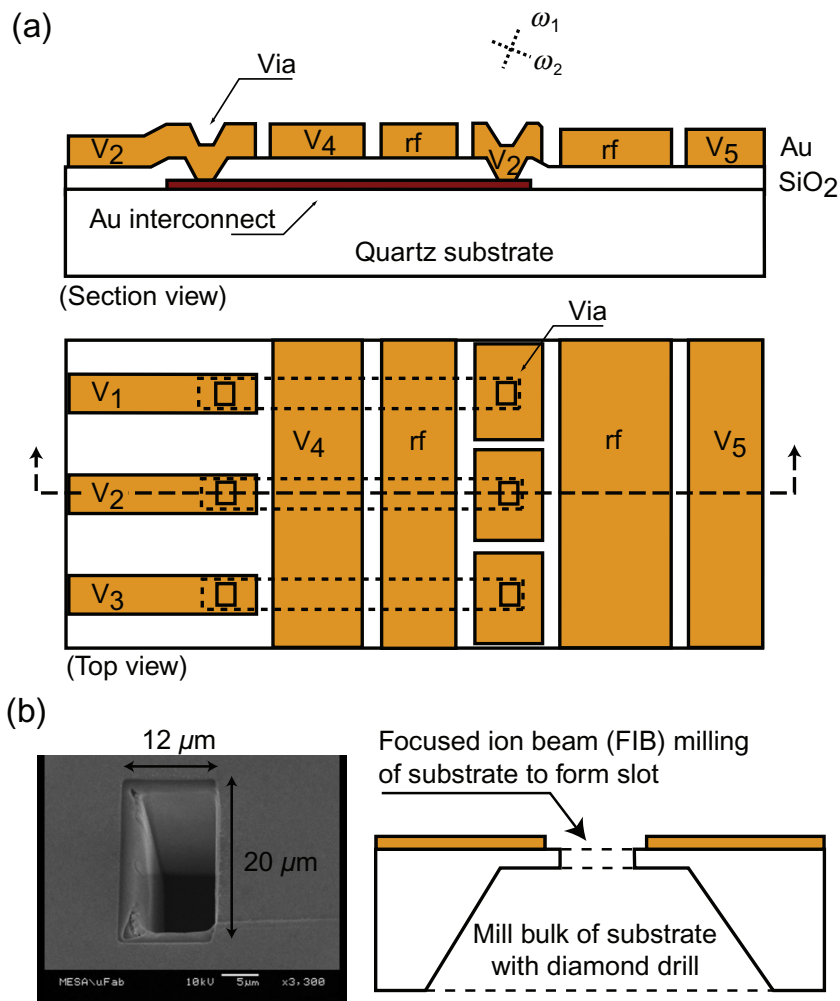
Figure 3. (a) Trap fabrication on a quartz substrate. The lower metal layer is evaporated gold (with titanium adhesion layers on both sides). The upper metal layer is evaporated gold with a titanium adhesion layer. The two metal layers are separated by a chemical-vapor-deposited silicon dioxide layer. The oxide layer is plasma etched to form vias between the layers. The rotated 'X' in the section view indicates the principal axes of the combined rf and control potential with the origin at the rf field null. (b) Backside loading slot. Neutral ^{24}Mg enters the trapping region from below through a slot in the quartz wafer and is then photoionized.

zones. The remaining $30\,\mu$m membrane was then milled using a focused ion beam to form a $12\,\mu$m by $20\,\mu$m slot in the surface connecting the drilled channel (figure 3(b)).

3. Trap geometry

The trap design, shown in figure 1(c), incorporates the use of a library of patterns that can be connected together to form more complex structures. The core of the trap design is the six Y junctions that are assembled to form a hexagonal ring. Two loading regions at either end

feed ions into the hexagonal ring. Inserted into two legs of the hexagon are components that can combine and separate pairs of ions for entangling and distributing the ions. Except for the loading regions, the outward legs of the hexagon are terminated in this design. However, these legs could be extended in future designs to integrate more hexagonal rings or other components such as memory storage regions.

Junctions between multiple ponderomotive tubes have been demonstrated in larger, multi-layer traps [9, 10], but these designs are not as convenient for scaling as the surface-electrode traps, in part because of the difficulty of alignment and assembly. An ideal junction would produce an rf ponderomotive zero at the axis of the ponderomotive confining tube along all three legs, merging in the junction center. Since such an exact ponderomotive zero is not possible for all points along the confining ponderomotive tube of a Y junction [13], we numerically optimized the shape of the rf rails in the junction (see section 3.2) to minimize the magnitude of the ponderomotive potential along a continuous path to the junction center. An iterative algorithm began with an initial shape (figure 4(a)) to generate the design shown in figure 4(c). Other choices for optimization criteria generate alternative junction geometries that might have benefits over the design that is used in this trap. For example, as shown in [10], efficient transport through a junction is possible even if the junction has large deviations from the ideal of an exact ponderomotive zero.

The control electrodes for the junction are narrow near the junction center for increased spatial control and some electrodes are connected on the surface to allow connections from other parts of the trap to pass under the junction. The final junction design was added to the component library for assembly into the hexagonal ring.

The limited number of available vacuum-feedthrough electrical connections available in our test apparatus required that single potentials be shared among multiple control electrodes. The loading zone and three junctions on the left half of the trap share 12 potentials distributed by the left-side control bus (figure 1(b)). The right-side loading zone and junctions have a similar control bus. The two experimental zones are independent of these buses and independent of each other. In this way, one set of control lines can be used to load and transport an ion while the experimental regions are configured to independently hold and manipulate other ions. A total of 48 separately controllable potentials were applied to the chip and distributed to the 150 control electrodes.

3.1. The design library

The trap geometry shown in figure 1(c) was assembled from a library of component designs. Each component has a specific function such as loading or transporting ions. A sample from this library is shown in figure 5. By developing and testing a component library, other trap designs can be assembled from the same library and use precalculated transport waveforms (see section 3.3). This components library includes connections to the control electrodes using the lower conducting layer. Standardizing the connections in this way greatly simplifies the design process since the connections tend to be very dense around complex components such as the junctions.

3.2. Electrode geometry optimization

The optimization procedure for the junction shape begins with a Y junction that has straight-edged rf electrodes, as shown in figure 4(a). The two rf rails in each arm of the Y junction
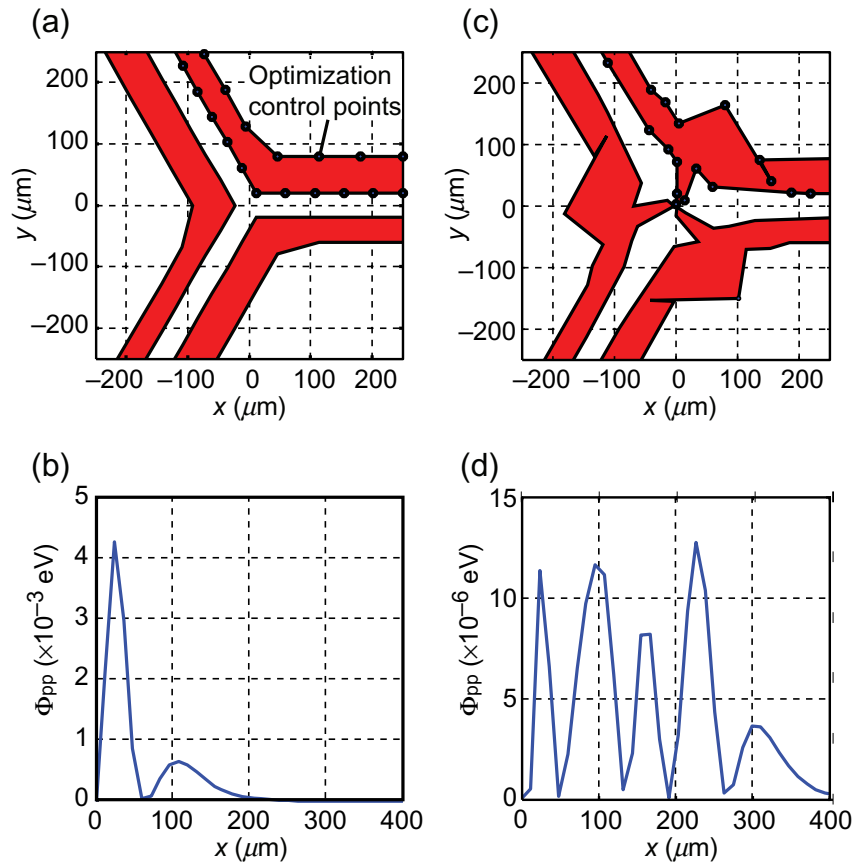
Figure 4. Optimization of junction rf electrodes (shown in red). (a) Initial shape used for optimization and (b) the ponderomotive potential Φ_{pp} at the center of the ponderomotive tube. The horizontal axes of (b) and (d) represent the position along the ponderomotive tube starting at the junction center ($x = 0$) and proceeding outward along the tube to the right. The ponderomotive potential is evaluated for the experimental conditions (51 V peak rf at 90.7 MHz and trapping ^{24}Mg^{+}). (c) Optimized junction shape and (d) its ponderomotive potential, which is 300 times smaller than the unoptimized case shown in (b).

have different widths, 40 and 60 μm, respectively, in order to rotate the rf quadrupole axis. This rotation simplifies the control potentials needed to allow a single laser beam, which is parallel to the electrode surface, to Doppler cool a trapped ion [16]. Close to the junction, the minimum value of the rf ponderomotive potential is not zero at every point along the center of the ponderomotive tube, but instead forms ponderomotive 'barriers', as shown in figures 4(b) and (d). The optimization objective was to find appropriate electrode shapes that minimized the absolute height of these barriers. The inner and outer edges of the initial electrodes are broken up into 16 line elements of roughly equal lengths. The locations of the points at which these line elements connect (shown as dots in figures 4(a) and (c)) serve as optimization parameters. The Nelder–Mead simplex optimization algorithm [17] was then used to systematically move these locations around in order to minimize the height of the barriers while maintaining the

Loading zone　　　Junction　　Experimental region　　Connection pads
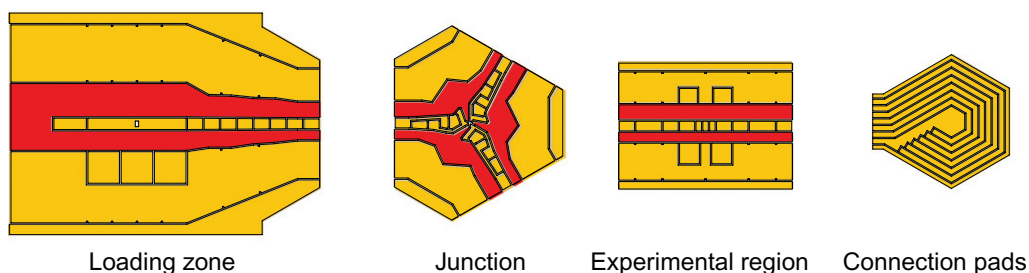
Figure 5. Example components from the design library. The components are assembled to form larger trapping structures such as the design detailed in this paper. Additional components provide standardized electrical connections on the lower conducting layer for the control electrodes. In the experimental regions, one zone on either side was elongated to provide storage zones. A narrow central electrode and additional electrodes outside the rf rails provide an electrical potential wedge for separating groups of ions as in [14, 15]. The shape of the connection pads was chosen to provide wide-angle access to various electrodes surrounding the pads.

threefold rotational symmetry of the junction. The algorithm uses the Biot–Savart-like law for two-dimensional electrostatic potentials derived in [18], which provides an analytical solution for the electric field contributions of any straight-line edge of a two-dimensional region at fixed potential and surrounded by a ground plane. Working with two-dimensional electrodes having straight-line edges therefore allows for rapid addition of the contributions due to the different edges. We also assume that the potential is specified everywhere on a two-dimensional plane, i.e. the gapless plane approximation [19–21]. Figure 4(c) illustrates the optimized electrode shapes and the corresponding ponderomotive barriers are shown in figure 4(d), achieving a suppression factor of greater than 300 over the initial ponderomotive barrier height in figure 4(b).

The shape of the rf rails was modified slightly to meet the constraints of our fabrication equipment including mitering of acute angles. The rf rails were then truncated at $270\,\mu$m from the junction center and encapsulated with control electrodes into a component for inclusion in the component library as shown in figure 6. The perimeter of the rf rails is listed in table 1. The ponderomotive barriers were calculated with the use of both the Biot–Savart-type integral in the gapless approximation and the use of a boundary element calculation. The resulting ponderomotive barriers are shown in figure 7(a) and an ion height above the surface is given in figure 7(b). As expected the ponderomotive trapping frequencies become weaker close to the center of the junction, as shown in figure 7(c). The boundary element calculation includes the effect of the gaps between the electrodes and the effect of the lower conducting layer as it passes under the gaps.

The control electrodes were designed once the rf electrodes shapes were determined. For adequate control along the ponderomotive tubes in the straight transport sections, the control electrodes were divided into $60\,\mu$m long segments (roughly 1.5 times the ion/surface distance). Near the junction, the control electrodes were designed with narrower electrodes to increase the spatial control of the potentials. The junction design also allows connections from the inside of the hexagonal ring to the outside to pass under the control electrodes.
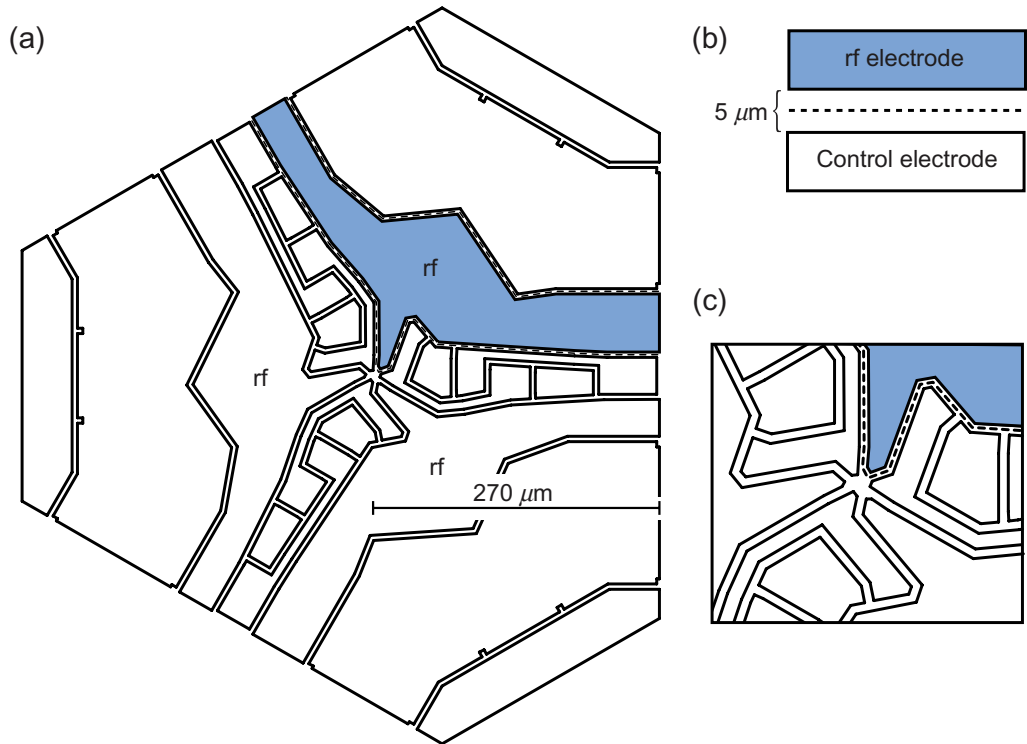
Figure 6. (a) The junction design used in the component library. The coordinates given in table 1 correspond to the dashed line around the shaded rf rail. (b) This perimeter is centered on the 5 μm gap between the rf rail and the control electrodes. (c) Detail of the center of the junction.

3.3. Transport waveforms

We apply time-dependent potentials (waveforms) to the control electrodes to transport the ions along the ponderomotive tube. The process of generating these waveforms begins with a calculation to determine a set of points, $\mathbf{x}_{center}$, that trace out the center of the ponderomotive tube and are separated by 1 μm intervals along the region the ion is to be transported. The goal then is to find, for each of the points in the set $\mathbf{x}_{center}$, the appropriate control electrode potentials that trap the ion in a harmonic potential well centered at that point. The potentials are constrained to not displace the ion transversely to the tube, where it will experience rf micromotion [16]. Smoothly switching between the potentials that give rise to wells centered at successive points along the ponderomotive tube will then form a waveform that transports the ion along the tube.

The process of calculating these potentials is divided into two steps for each of the 1 μm spaced locations, say the point $\mathbf{x}_{center}^{(i)}$. In the first step, we use constrained linear programming optimization to ensure that the control electrode potentials do not create an electric field at $\mathbf{x}_{center}^{(i)}$. Given n participating control electrodes, let $\mathbf{A}$ represent the $3 \times n$ matrix containing in the jth column the contributions to the electric field component at $\mathbf{x}_{center}^{(i)}$ in the x, y and z directions, respectively, if the jth electrode is held at 1 V and all others at 0 V. The null space of $\mathbf{A}$ then gives a set of $n-3$ vectors $\mathbf{v}$, each satisfying the condition $\mathbf{Av} = 0$, i.e. the entries in each vector $\mathbf{v}$ give a combination of potentials that may be applied to the n electrodes without producing an electric field at $\mathbf{x}_{center}^{(i)}$. The desired potential well may be constructed from a linear combination

Table 1. Coordinates along the perimeter of one of the junction's three rf rails after the optimized shape was modified for inclusion in the design library (see the text and figure 6(a)). The 5 μm gap between the rf and control electrodes was centered on this perimeter, cutting equally into both sets of electrodes as shown in figure 6(b). The other two rails can be obtained from these coordinates by rotations of 120° and 240° about the origin.

Vertex	x (μm)	y (μm)
1	270.0	80.0
2	172.0	80.0
3	134.5	74.7
4	80.1	155.9
5	7.8	148.9
6	−39.7	188.8
7	−84.3	266.0
8	−118.9	246.0
9	−91.4	198.4
10	−42.7	124.6
11	−13.0	90.7
12	1.8	70.0
13	2.0	19.7
14	1.2	8.5
15	4.0	3.4
16	14.9	7.1
17	31.4	52.3
18	38.1	53.6
19	58.8	29.7
20	189.7	21.3
21	220.4	20.0
22	270.0	20.0

of these vectors while maintaining the zero field condition. We also constrain the potentials to be in the range ±5 V, which is within the range our control electronics can generate.

In the second step, the potential well of the desired trapping frequency, and centered on $\mathbf{x}_{\text{center}}^{(i)}$, is now generated from a linear combination of the above solutions. We use a Nelder–Mead simplex optimization algorithm [17], which varies the contribution of each null space vector in such a linear combination. In each iteration the potential due to the current linear combination of null space vectors is calculated at ten points along the tube, extending over ±50 μm from the well center. The algorithm minimizes the root-mean-square difference between the calculated potential and a target harmonic potential. This method of fitting to the ±50 μm interval ensures that the well has sufficient depth along the rf tube. During the calculation we ignore the effect of the applied potentials on the trapping in the radial direction. However, choosing the control electrode target potential to have a trapping frequency significantly smaller than the local radial ponderomotive trapping frequencies ensures that the potential does not become anti-trapping in the radial direction. We post-check that this is indeed the case, and that the trap has sufficient depth in all directions.
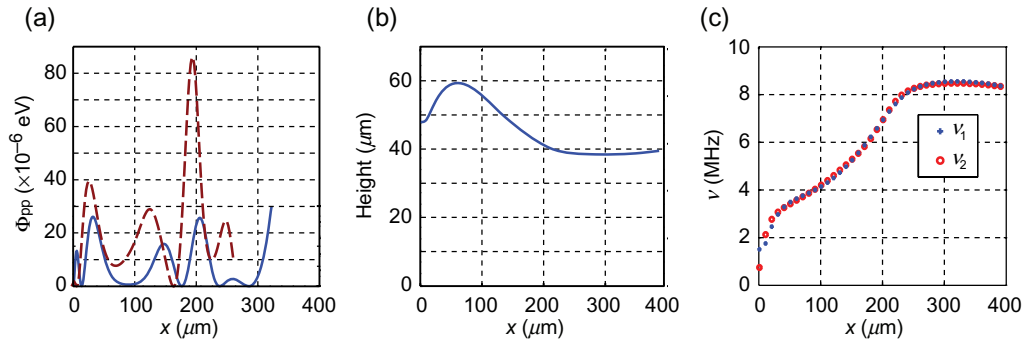
Figure 7. Trapping characteristics of the final junction design (junction center located at $x = 0$). (a) Ponderomotive barriers calculated (solid line) using the Biot–Savart-like boundary integrals in the gapless approximation and (dashed line) using a boundary element code to calculate the potentials including $5\,\mu$m gaps between the electrodes and the lower layer interconnects (see the text). The boundaries in the calculations are defined by the coordinates given in table 1. The ponderomotive potential is evaluated for the experimental conditions (51 V peak rf at 90.7 MHz and trapping ^{24}Mg$^+$). The ponderomotive barrier rising to the right of $x = 300\,\mu$m does not affect transport in the vicinity of the junction. It is caused by the adjacent loading zone, which has been included in this calculation. (b) Ion height as a function of position. (c) Ponderomotive radial trapping frequencies as a function of position.

Ideally the potentials calculated by the above method would vary smoothly as the ion is transported along the ponderomotive tube, but we find that the algorithm intermittently produced sharp, unwanted jumps in the potentials that form wells centered on successive $\mathbf{x}_{\text{center}}^{(i)}$. These jumps most likely occur because all $n = 14$ independent control electrodes were included in our optimization for precise specification of the potential at many points, therefore allowing many different, equally viable optimized solutions. To remove these jumps, the potentials are post-smoothed by replacing the potentials associated with a well centered on $\mathbf{x}_{\text{center}}^{(i)}$ by the average of the potentials associated with the two nearest neighboring wells, i.e. those wells centered on $\mathbf{x}_{\text{center}}^{(i-1)}$ and $\mathbf{x}_{\text{center}}^{(i+1)}$. This averaging can be repeated several times, first for all $\mathbf{x}_{\text{center}}^{(i)}$ where i is odd and then for all $\mathbf{x}_{\text{center}}^{(i')}$ where i' is even, and so on. After ten levels of smoothing the zero-field condition at each well center is only weakly violated. We estimate this violation to be no greater than that caused by uncertainties in the trap fabrication, which limits the precision with which we can specify the location of the tube center to within $1\,\mu$m.

4. Results

To test the basic features of the trap, ^{24}Mg$^+$ ions were loaded by photoionizing (285 nm) a neutral flux of ^{24}Mg created in a resistively heated oven. To prevent contamination and possible shorting of the trap electrodes by the neutral flux, the oven was located behind the chip (as viewed in figures 1(b) and (c)). Some of the flux then enters the loading regions through two $12\,\mu$m by $20\,\mu$m slots (see figure 3(b)). From 1 to 10 ions were typically loaded, depending on the loading duration, neutral flux, and photoionization intensity. The ponderomotive potential is significantly perturbed in the vicinity of the loading slots, primarily because the dielectric

quartz distorts the rf electric field. After loading, the ions were located $20\,\mu$m to the side of the slot (along the axis) due to this perturbation.

The trap was enclosed in a vacuum chamber that had several glass viewports for laser access and for imaging the ions. The viewport used for the imaging was 6.5 cm in diameter and located 2.5 cm above the trap surface. We suspect that photoelectrons emitted from the trap surface by the photoionization beam and the Mg^+ Doppler cooling beams (280 nm) were charging the glass in the viewport. This apparent charging prevented the trap from holding ions without applying strong compensation fields using the control electrodes. The timescale for the charging was minutes, while discharging required several hours. To mitigate this problem, we installed a grounded gold screen ($42\,\mu$m spacing with 83% light transmission) 5 mm above the trap, parallel to the surface. At this distance, the screen does not significantly affect the trap potentials but it greatly reduced the apparent charging effects [22].
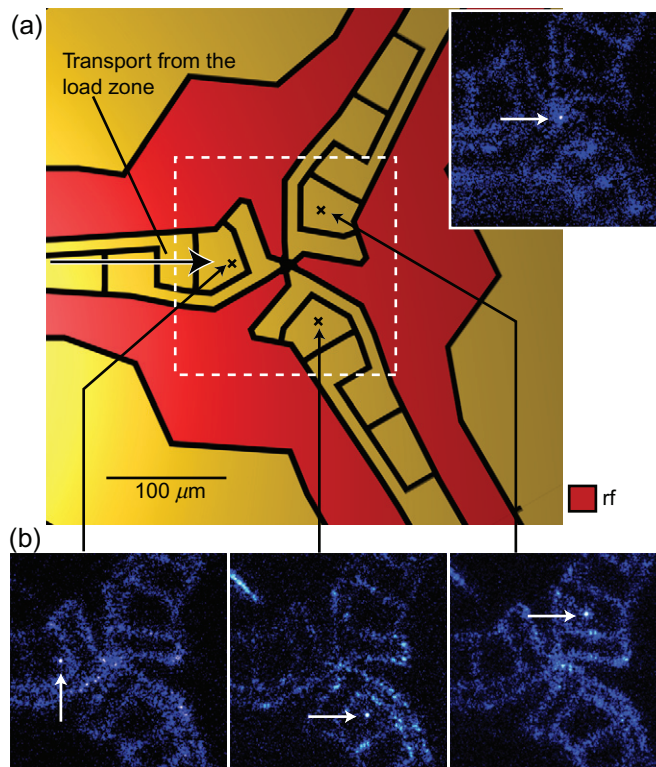
4.1. Transport

Ions were successfully loaded in both loading regions of the trap and transported to and through the first adjacent Y junction, as shown in figure 8. We transported individual or groups of ions $850\,\mu$m from the loading zone to the leg of the junction in 2 ms (figure 8(a)). Potentials applied to the control electrodes then transfer the ion to either of the other two legs. Figure 8(b) shows a trapped ion in three locations around the leftmost junction of figure 1. We were able to transport ions between any pair of the junction's three legs and in any order. We also transported ions to the center of the junction directly from the loading zone, as shown in figure 8(a).

In these preliminary experiments, we were unable to use the calculated waveforms for adiabatic transport between the junction's legs because of unexpected barriers to the ion transport around $30\,\mu$m from the junction center. Instead, this part of the transport used a waveform that initially generated a symmetric set of three wells, one on each leg. During transport, the control potentials were adjusted briefly to form a single well on one leg with a barrier on all three legs that prevented the ion from exiting the vicinity of the junction. The ion then Doppler cools into the single well. Finally, the original symmetric three-well potential was restored with the ion in the new position.

Transport between the legs in this initial test was thus ballistic and required that a laser cooling beam overlap the final location of the transport in each leg. The overlap of these cooling beams covered much of the junction and the cooling was applied continuously during transport. This is in contrast to the ion transport through a junction demonstrated in both [9, 10], where the transport was not assisted by laser cooling. Stray fields, varying over the course of a day, also made the transport erratic. With careful adjustment of the waveforms, an ion could be transported around the legs of the junction dozens of times before being lost. Transport loss is expected to be high due to the large ion heating from this type of transport. Transport between two of the junctions seemed technically feasible but practically difficult because of the need for continual adjustment of the waveform to compensate for time varying charging fields. We did transport ions just past the midpoint between two of the junctions. However, much of the work with this trap has been focused on determining the source of the barrier and the stray fields, which is still not understood.

For a further demonstration of transport through this junction, please see the online supplementary material for this paper, available at stacks.iop.org/NJP/12/033031/mmedia. The included video shows a consecutive sequence of six transports clockwise around the junction followed by six transports counterclockwise.

Figure 8. (a) Diagram of a Y junction with an inset showing an ion trapped in the junction center. (b) Transport through the leftmost Y junction shown in figure 1. Each photo (false color) shows an ion in one of three locations around the junction. All ions were transported to the junction from a load zone attached to the junction's left leg. To illustrate the electrode locations in the photos, a laser beam was directed at the quartz substrate so that the scattered light illuminates the gaps between the electrodes.

4.2. The heating rate

One characteristic parameter of an ion trap is the *in situ* heating rate of the ions due to fluctuating electric fields at the ion location. Typically, miniature rf Paul traps have observed heating rate orders of magnitude greater than expected from simple Johnson noise on the control electrodes [16, 23, 24]. The source of these noisy electric fields is still not understood, but they can be approximately characterized according to ion–electrode distance. The heating rate for a single ion at the location shown in figure 1(c) was observed to be $\dot{n} = 87(11) \times 10^3$ phonon s^{-1} at a 3.5 MHz axial frequency and a 38 μm ion-to-surface distance, using the recooling method described in [24]. The corresponding electric field noise spectral density seen by the ion is $S_E(\omega) \approx \dot{n}(4m\hbar\omega/e^2) \approx 1.3(2) \times 10^{-9}$ V^2 m^{-2} Hz^{-1} [24–26], where m and e are the ion mass and charge, respectively. This places this trap in the average range of heating rates for its size scale.

We also characterized a separate linear surface-electrode trap made with 1 μm thick electroplated gold. This trap demonstrated transport over 20 zones (greater than 1 mm travel) and, as with the hexagonal trap, used multiple conducting layers for interconnects. The linear

trap was designed with a subset of the component library used for the trap of figure 1. The heating rate in this trap gave $S_E(\omega) < 6 \times 10^{-11}\,\mathrm{V^2\,m^{-2}\,Hz^{-1}}$ as determined by the axial heating of a $^{24}\mathrm{Mg}^+$ ion at 4.5 MHz and 40 μm ion–electrode distance using the recooling method. This bound is more than an order of magnitude lower than the evaporated gold trap.

The relatively low heating measured for the electroplated-gold surface-electrode trap described in [8] as compared to other traps of similar dimensions has elicited conjecture that electroplated gold might have low heating rates in general. The results from the linear trap reported here further support this conjecture, but given the wide variation in heating rates measured between traps of similar materials, we cannot draw a definitive conclusion from these measurements.

5. Conclusions

The remaining issues that need to be investigated with this type of trap include the sources of stray electric fields and apparent discrepancies between the observed ion positions and those predicted from potential calculations. The design components are not limited to the gold-on-quartz construction and could be realized with other choices of materials and fabrication processes. Different strategies for electrode geometry optimization should also be explored. We expect that as the component library is refined and expanded, the design and construction of ion traps for future quantum information processing experiments will become considerably faster and more reliable.

References

[1] Blatt R and Wineland D 2008 Entangled states of trapped atomic ions *Nature* **453** 1008–15
[2] Monroe C and Lukin M 2008 Remapping the quantum frontier *Phys. World* 32–39
[3] Häffner H, Roos C F and Blatt R 2008 Quantum computing with trapped ions *Phys. Rep.* **469** 155–203
[4] Kielpinski D, Monroe C and Wineland D 2002 Architecture for a large-scale ion-trap quantum computer *Nature* **417** 709–11
[5] Kim J, Pau S, Ma Z, McLellan H R, Gates J V, Kornblit A, Slusher R E, Jopson R M, Kang I and Dinu M 2005 System design for large-scale ion trap quantum information processor *Quantum Inf. Comput.* **5** 515–37
[6] Steane A M 2007 How to build a 300 bit 1 gig-operation quantum computer *Quantum Inf. Comput.* **7** 171–83
[7] Chiaverini J, Blakestad R B, Britton J, Jost J D, Langer C, Leibfried D, Ozeri R and Wineland D 2005 Surface-electrode architecture for ion-trap quantum information processing *Quantum Inf. Comput.* **5** 419–39
[8] Seidelin S *et al* 2006 Microfabricated surface-electrode ion trap for scalable quantum information processing *Phys. Rev. Lett.* **96** 253003

[9] Hensinger W K, Olmschenk S, Stick D, Hucul D, Yeo M, Acton M, Deslauriers L, Monroe C and Rabchuk J 2006 T-junction ion trap array for two-dimensional ion shuttling storage and manipulation *Appl. Phys. Lett.* **88** 034101

[10] Blakestad R B, Ospelkaus C, VanDevender A P, Amini J M, Britton J, Leibfried D and Wineland D J 2009 High-fidelity transport of trapped-ion qubits through an X-junction trap array *Phys. Rev. Lett.* **102** 153002

[11] Leibrandt D R *et al* 2009 Demonstration of a scalable, multiplexed ion trap for quantum information processing *Quantum Inf. Comput.* **9** 901

[12] Jaeger R C 2002 *Introduction to Microelectronic Fabrication (Modular Series on Solid State Devices* vol 5*)* 2nd edn (Englewood-Cliffs, NJ: Prentice-Hall)

[13] Wesenberg J H 2009 Ideal intersections for radio-frequency trap networks *Phys. Rev.* A **79** 013416

[14] Barrett M D *et al* 2004 Deterministic quantum teleportation of atomic qubits *Nature* **429** 737

[15] Jost J D, Home J P, Amini J M, Hanneke D, Ozeri R, Langer C, Bollinger J J, Leibfried D and Wineland D J 2009 Entangled mechanical oscillators *Nature* **459** 683

[16] Amini J M, Britton J, Leibfried D and Wineland D J 2009 Microfabricated chip traps for ions *Atom Chips* ed J Reichel and V Vuletic (New York: Wiley-VCH) at press (arXiv:0812.3907)

[17] Press W H, Teukolsky S A, Vetterling W T and Flannery B P 2002 *Numerical Recipes in C++: The Art of Scientific Computing* 2nd edn (Cambridge: Cambridge University Press)

[18] Oliviera M H and Niranda J A 2001 Biot-Savart-like law in electrostatics *Eur. J. Phys.* **22** 31

[19] Wesenberg J H 2008 Electrostatics of surface-electrode ion traps *Phys. Rev.* A **78** 063410

[20] House M G 2008 Analytic model for electrostatic fields in surface-electrode ion traps *Phys. Rev.* A **78** 033402

[21] Schmied R 2009 Electrostatics of gapped and finite surface electrodes arXiv:0910.4517

[22] Pearson C E, Leibrandt D R, Bakr W S, Mallard W J, Brown K R and Chuang I L 2006 Experimental investigation of planar ion traps *Phys. Rev.* A **73** 032307

[23] Deslauriers L, Haljan P C, Lee P J, Brickman K A, Blinov B B, Madsen M J and Monroe C 2004 Zero-point cooling and low heating of trapped Cd+ 111 ions *Phys. Rev.* A **70** 043408

[24] Epstein R J *et al* 2007 Simplified motional heating rate measurements of trapped ions *Phys. Rev.* A **76** 033411

[25] Turchette Q A *et al* 2000 Heating of trapped ions from the quantum ground state *Phys. Rev.* A **61** 063418

[26] Labaziewicz J, Ge Y, Antohi P, Leibrandt C, Brown K R and Chuang I L 2008 Suppression of heating rates in cryogenic surface-electrode ion traps *Phys. Rev. Lett.* **100** 013001